Nanoscale

PAPER

View Article Online
View Journal | View Issue

Cite this: *Nanoscale*, 2021, **13**, 19023

Multimodal fluorescently labeled polymer-coated GdF_3 nanoparticles inhibit degranulation in mast cells†

Oleksandr Shapoval, *[a] Vadym Sulimenko,[b] Anastasiya Klebanovych,[b] Mariia Rabyk,[a] Pavlo Shapoval,[c] Ondřej Kaman,[d] Eliška Rydvalová,[a] Marcela Filipová,[a] Eduarda Dráberová,[b] Pavel Dráber *[b] and Daniel Horák *[a]

Multimodal gadolinium fluoride nanoparticles belong to potential contrast agents useful for bimodal optical fluorescence and magnetic resonance imaging. However, the metallic nature of the nanoparticles, similarly to some paramagnetic iron oxides, might induce allergic and anaphylactic reactions in patients after administration. A reduction of these adverse side effects is a priority for the safe application of the nanoparticles. Herein, we prepared paramagnetic poly(4-styrenesulfonic acid-*co*-maleic acid) (PSSMA)-stabilized GdF_3 nanoparticles with surface modified by Atto 488-labeled poly(styrene-*grad*-2-dimethylaminoethyl acrylate)-*block*-poly(2-dimethylaminoethyl acrylate) (PSDA-A488) with reactive amino groups for introduction of an additional imaging (luminescence) modality and possible targeting of anticancer drugs. The saturation magnetization of GdF_3@PSSMA particles according to SQUID magnetometry reached 157 $Am^2\ kg^{-1}$ at 2 K and magnetic field of 7 T. GdF_3@PSSMA-PSDA-A488 nanoparticles were well tolerated by human cervical adenocarcinoma (HeLa), mouse bone marrow-derived mast cells (BMMC), and rat basophilic mast cells (RBL-2H3); the particles also affected cell morphology and protein tyrosine phosphorylation in mast cells. Moreover, the nanoparticles interfered with the activation of mast cells by multivalent antigens and inhibited calcium mobilization and cell degranulation. These findings show that the new multimodal GdF_3-based nanoparticles possess properties useful for various imaging methods and might minimize mast cell degranulation incurred after future nanoparticle diagnostic administration.

Received 17th September 2021,
Accepted 3rd November 2021

DOI: 10.1039/d1nr06127e

rsc.li/nanoscale

Introduction

Rare-earth fluoride nanoparticles containing 4f electrons have recently attracted a great deal of attention due to their unique electronic, chemical, and optical characteristics and good chemical stability. In particular, lanthanide fluoride particles are finding interesting applications in X-ray therapy or fluorescence and magnetic resonance imaging (MRI).[1–4] However, optical microscopy and MRI suffer from some limitations. While *in vivo* optical fluorescence imaging provides only limited quantitative analysis, its integration with highly sensitive 3D tomographic MRI in one system represents an interesting approach complementing high resolution and accuracy of fluorescence analysis with a high penetration depth of MRI. This enables fluorescence-guided surgery[5] and noninvasive imaging of living subjects with high sensitivity and accuracy and good resolution.[6]

Recently, gadolinium fluorides with various morphologies (shape, particle size, and dispersity) and specific luminescent properties have been synthesized by changing reaction conditions using numerous methods, including thermal decomposition, two-phase liquid–solid approaches, coprecipitation, hydrothermal methods, reverse micelle techniques, and microwave irradiation.[7,8] Typically, the morphology and size of nanoparticles were controlled by using different stabilizing agents.[4,9,10] This approach produced highly crystalline particles with desirable purity, narrow size distribution without aggregation, and required surface charge, which has a great impact on protein adsorption and prediction of *in vivo* particle behavior. The advantage of GdF_3 nanoparticles consisted in their biocompatibility, having negligible cytotoxicity, which

[a]*Institute of Macromolecular Chemistry of the Czech Academy of Sciences, Heyrovského nám. 2, 162 06 Prague 6, Czech Republic*
[b]*Laboratory of Biology of Cytoskeleton, Institute of Molecular Genetics of the Czech Academy of Sciences, Vídeňská 1083, 142 20 Prague 4, Czech Republic*
[c]*Department of Physical, Analytical and General Chemistry, Lviv Polytechnic National University, Sv. Yura Sq. 9, 79013 Lviv, Ukraine*
[d]*Institute of Physics of the Czech Academy of Sciences, Cukrovarnická 112/10, 162 00 Prague 6, Czech Republic*

†Electronic supplementary information (ESI) available. See DOI: 10.1039/d1nr06127e

makes them suitable for biomedical applications.[11,12] GdF_3 nanoparticles provided promising results also due to their good dispersibility in a range of solvents, high mass relaxivity (*i.e.*, short proton relaxation time in MRI), and easy surface modifications enabling to regulate cellular uptake, trafficking, and export, required by a specific biomedical application.[13] Nanoparticles coated with biological ligands triggered specific cell signaling responses and enhanced the ability to crosslink cell surface receptors. As an example, anionic bifunctional Eu^{3+}-doped Gd_2O_3 nanoparticles modified with citric acid or rhodamine-containing paramagnetic gadolinium particles efficiently labeled tumor cells.[14] The particles modified with targeting agents were found useful for *in vivo* trafficking of the metastatic, stem, and immune cells.[15] Gd-based particles also induced maturation of dendritic cells that have a pivotal role in host immune defense, such as elimination of foreign pathogens and inhibition of tumorigenesis.[16] However, whether the Gd-based nanoparticles can affect activity of mast cells, which play a pivotal role in allergic reactions, anaphylaxis, as well as in immune tolerance, is unknown.

Mast cells are typically located at body-environment interfaces and may be found in close vicinity of blood vessels, peripheral nerves, mucosal membranes, skin, and subcutaneous tissue. Hence, they are one of the first immune cells likely to encounter and respond to a foreign material exposure initiating the inflammatory response.[17] Mast cells express plasma membrane-associated high-affinity IgE receptors (FcεRIs), the aggregation of which by multivalent antigen (Ag)-IgE complex triggers activation pathway leading to tyrosine phosphorylation of the FcεRI β- and γ-subunits. This is followed by enhanced activity of Src and Syk tyrosine kinase families and phosphorylation of transmembrane adaptors that coordinate further signal propagation resulting in Ca^{2+} influx across the plasma membrane. Activation events culminate in the release of preformed granule mediators and *de novo* synthesis and secretion of bioactive compounds.[18] The action of these mediators is clinically observed as immediate and late-phase allergic reactions. Besides that, mast cell activation by FcεRI aggregation is accompanied by changes in cell morphology and enhanced cell adhesion and migration.[19] The interaction of metal-based nanoparticles with mast cells is an emerging new field in the investigation of signaling and cellular responses during activation events and the effect of physicochemical properties of the particles on mast cell responses needs to be investigated. For example, ZnO and TiO_2 nanoparticles inhibited or stimulated mast cell degranulation after FcεRI crosslinking, respectively.[20] The degranulation was also induced by 5 nm Ag nanoparticles, but not by 100 nm ones,[21] while 20 nm Ag nanoparticles increased intracellular Ca^{2+} level and degranulation in a FcεRI-independent manner.[22] Functionalized Au nanoparticles blocked IgE-dependent degranulation.[23] It was also interesting to note that ionic Gd^{3+} chelate contrast agents induced the release of histamine from mast cells.[24] When free ionic groups were blocked by methylamide, the Gd^{3+} toxicity was entirely suppressed. Therefore, it is important to examine the response of the immune system on the GdF_3 nanoparticles, which can distinctively affect mast cell viability and degranulation.

In the present work, we focused on the design of GdF_3 nanoparticles by a facile coprecipitation of gadolinium chloride and NH_4F from ethylene glycol with poly(4-styrenesulfonic acid-*co*-maleic acid) (PSSMA) stabilizer. Fluorophore-labeled poly(styrene-*grad*-2-dimethylaminoethyl acrylate)-*block*-poly(2-dimethylaminoethyl acrylate) copolymer was used as a coating that conferred additional functionalities to the particles, especially, luminescence, biocompatibility, and possible capability to deliver drugs. The new multimodal particles were thoroughly characterized in terms of their physicochemical properties and magnetic measurements, *in vitro* cytotoxicity on cell lines, and interference with activation of mast cells, playing a pivotal role in allergy, inflammation, and innate immunity.

Experimental

Materials

Gadolinium(III) chloride hexahydrate (99.9%), ammonium fluoride, phosphate-buffered saline (PBS), xylenol orange, Triton X-100, HEPES, dinitrophenyl-albumin (DNP-albumin), 4-nitrophenyl *N*-acetyl-β-D-glucosaminide (4-NAG), 2-ethoxy-1-ethoxycarbonyl-1,2-dihydroquinoline (EEDQ), 4,4′-azobis(4-cyanovaleric acid) (ACVA), *N*-hydroxysuccinimide (NHS) ester of Atto 488 (denoted as A488) fluorescent dye, piperidine, and *N*,*N*-dimethylacetamide (DMAc) were purchased from Sigma-Aldrich (St. Louis, MO, USA). Sodium salt of poly(4-styrenesulfonic acid-*co*-maleic anhydride) (PSSMA; M_w = 20 000 g mol^{-1}) was obtained from Scientific Polymer Products (Ontario, NY, USA). *N*-(9-Fluorenylmethyloxycarbonyl)-ethylenediamine hydrochloride (Fmoc-EDA) was purchased from Iris Biotech (Marktredwitz, Germany). Rhodamine phalloidin stain kit, wheat germ agglutinin (WGA) Alexa Fluor 555 conjugate, Hoechst 33342, and FluoroBrite™ DMEM were from Thermo Fisher Scientific (Waltham, MA, USA). Poly(styrene-*grad*-2-dimethylaminoethyl acrylate)-*block*-poly(2-dimethylaminoethyl acrylate) [$P(S_{0.5}$-*grad*-$DMAEA_{0.5})_{70}$-*b*-$PDMAEA_{50}$; PSDA] (Scheme 1) was synthesized by nitroxide-mediated radical polymerization.[25] Fura-2-acetoxymethyl ester (Fura-2-AM) was purchased from Invitrogen (Carlsbad, CA, USA). For the degranulation, Tyrode's buffer (112 mM NaCl, 2.7 mM KCl, 0.4 mM

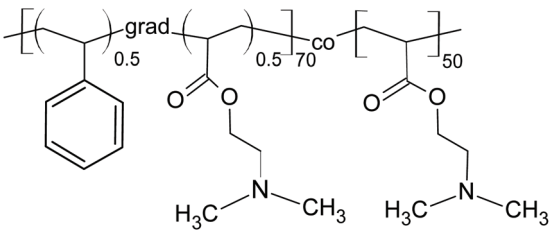

Scheme 1 Poly(styrene-*grad*-2-dimethylaminoethyl acrylate)-*block*-poly(2-dimethylaminoethyl acrylate) (PSDA).

NaH_2PO_4, 1.6 mM $CaCl_2$, 1 mM $MgCl_2$, 5.6 mM glucose, 10 mM HEPES, pH 7.4, 0.1% bovine serum albumin) was used. Ethanol, toluene, ethylene glycol (EG), dimethyl sulfoxide (DMSO), and ammonium hydroxide (25%) were obtained from Lachema (Brno, Czech Republic). All chemicals were used directly without further purification. Ultrapure Q-water ultrafiltered on a Milli-Q Gradient A10 system (Millipore; Molsheim, France) was used in all experiments.

Labeling of PSDA with A488 fluorescent dye

Synthesis of Atto 488-labeled poly(styrene-*grad*-2-dimethylaminoethyl acrylate)-*block*-poly(2-dimethylaminoethyl acrylate) is schematically shown in Scheme 2. Briefly, PSDA (3.78 g; 0.261 mmol) was dissolved in anhydrous toluene (50 ml) at 115 °C with continuous stirring and ACVA (1.46 g; 5.2 mmol) solution in anhydrous DMAc (6 ml) was added in three portions. The reaction mixture was kept at 115 °C for another 3 h, cooled down, and purified by dialysis (MWCO 3500 Da) against water for 72 h. The resulting PSDA-COOH was washed with *n*-heptane (60 ml) and the aqueous layer was lyophilized. Yield: 2.95 g.

PSDA-COOH (2.83 g) was dissolved in DMAc (20 ml) and the solution of EEDQ (0.48 g; 10 mol excess relative to PSDA-COOH) in DMAc (5 ml) was added at room temperature (RT) with continuous stirring. Separately, Fmoc-EDA (0.18 g; 3.2 mol excess relative to PSDA-COOH) was dissolved in DMAc (5 ml) at 60 °C and added to the PSDA-COOH solution in two portions. The reaction mixture was stirred at RT overnight, heated at 65 °C for 2 h, and resulting PSDA-Fmoc was washed with *n*-heptane (50 ml), dialyzed against water (pH 3) for 48 h (MWCO 3500 Da), and lyophilized; yield: 2.65 g. PSDA-Fmoc (2.55 g) was dissolved in anhydrous DMAc (20 ml), piperidine (30 ml) was added, and the mixture was stirred at RT for 3 h. The resulting PSDA-NH_2 was purified by dialysis (MWCO 3500 Da) against water (pH 4) for 48 h and lyophilized.

Finally, PSDA-NH_2 was decorated with A488 fluorescence label. Briefly, PSDA-NH_2 (1 g) was dissolved in DMSO (15 ml), NHS ester of A488 (2 mg) was added and the reaction mixture was stirred at RT for 10 h, dialyzed (MWCO 3500 Da) against water for 72 h, and lyophilized. The resulting polymer was denoted as PSDA-A488; yield: 0.59 g. The content of fluorescent label (0.2 wt%) in PSDA-A488 was determined spectrophotometrically at 502 nm.

Synthesis of PSSMA- and EG-stabilized GdF_3 nanoparticles

GdF_3 nanoparticles were prepared by a coprecipitation method in EG. In a typical procedure, $GdCl_3{\cdot}6H_2O$ (5 mmol) and PSSMA (0–15 mg ml^{-1}) were dissolved in EG (20 ml) with magnetic stirring, solution of NH_4F (5 mmol) in EG (10 ml) was added dropwise, and the reaction mixture was kept at 75 °C for 3 h with stirring. The solution was cooled to RT, resulting GdF_3 precipitate was separated by centrifugation (6000 rpm) for 30 min, washed with water and ethanol several times, and stored in water. Before physicochemical analyses, the particle dispersion was dried at RT for 24 h under vacuum. The PSSMA-stabilized GdF_3 nanoparticles and the particles prepared in EG as a solvent and capping agent in the absence of PSSMA were denoted as GdF_3@PSSMA and GdF_3@EG particles, respectively.

Surface modification of GdF_3@PSSMA nanoparticles with PSDA-A488

Aqueous GdF_3@PSSMA dispersion (500 μl; 1 mg ml^{-1}) was mixed with aqueous PSDA-A488 solution (1 ml; pH 11) with shaking for 30 min and continuous stirring at RT overnight, which was followed by centrifugation (12 000 rpm) for 10 min. The resulting GdF_3@PSSMA-PSDA-A488 particles were washed and resuspended in water to the desired concentration.

Characterization of nanoparticles

Particle morphology was examined by a Philips 200CM transmission electron microscope (TEM). Particle size distribution was obtained by counting several hundreds of particles from the TEM micrographs and by dynamic light scattering (DLS) measurements (Zetasizer NanoZS90; Malvern, UK). While the former method determines the number (D_n)- and weight-average particle diameter (D_w) and dispersity ($Đ = D_w/D_n$) characterizing the particle size distribution, the latter technique measures the hydrodynamic diameter D_h and polydispersity PD. X-ray diffraction (XRD) patterns of the particles were

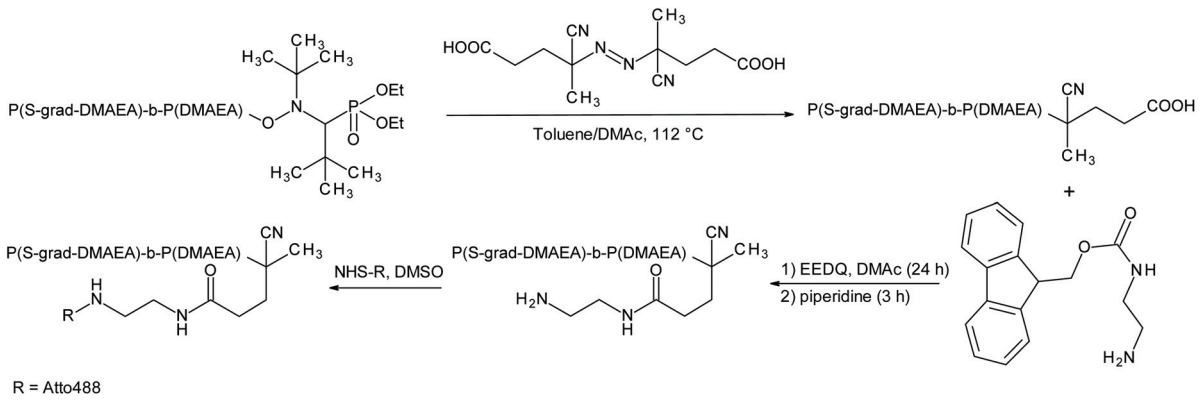

Scheme 2 Synthesis of Atto 488-labeled poly(styrene-*grad*-2-dimethylaminoethyl acrylate)-*block*-poly(2-dimethylaminoethyl acrylate).

obtained on a Bruker D8 diffractometer with a scintillation detector and analyzed by the Rietveld method in FullProf program. The mean size of crystallites (D_{XRD}) was evaluated from peak broadening, for which the Thompson–Cox–Hastings pseudo-Voigt profile was applied. The effect of instrumental broadening was determined by measuring a strain-free tungsten powder with the crystallite size of 9.4 μm. Anisotropic size models were based on an expansion of crystallite shape by spherical harmonics consistent with symmetry of respective phases. Fourier-transform infrared (FTIR) spectra in the attenuated total reflection (ATR) mode were obtained with a Thermo Nicolet NEXUS 870 spectrometer (Madison, WI, USA). The magnetic behavior of the particles was investigated in DC field using a Quantum Design MPMS XL superconducting quantum interference device (SQUID; San Diego, CA, USA). Magnetization curves were recorded at 2 and 300 K up to the magnetic field of 7 T. The susceptibility scans were measured with cooling in applied magnetic field B = 0.1 T (H = 79.6 kA m^{-1}). Emission and excitation spectra were recorded on an FS5 Edinburgh Instruments spectrofluorometer (Edinburgh, UK) equipped with both continuous (150 W) and pulsed xenon lamps.

Leaching of Gd^{3+} ions from GdF_3@PSSMA-PSDA-A488 nanoparticles

The leaching of free Gd^{3+} from the particles was determined by spectrophotometry using xylenol orange as described early.[26] Briefly, an aqueous dispersion of GdF_3@PSSMA-PSDA-A488 nanoparticles (2 ml; 3.7 mM of Gd^{3+}) was stored at RT for 40 days, the nanoparticles were removed by centrifugation (14 000 rpm) for 30 min, the supernatant (0.15 ml) was mixed with xylenol orange buffer solution (1.5 ml, pH 5.8), and Gd^{3+} concentration was monitored by a UV-vis Specord 250 Plus UV-Vis spectrophotometer (Analytik Jena; Germany) at 350–650 nm. A calibration curve was obtained using aqueous $GdCl_3$ solutions (0–70 μM Gd^{3+}) and acetate buffer solution (pH 5.8) according to the procedure described earlier.[27] The concentration of free Gd^{3+} was directly proportional to the absorbance ratio at 573 and 433 nm.

Cell cultures and activation

Rat basophilic leukemia cell line RBL-2H3 (cat. no. CRL-2256; RBL), representing a model for mast cell activation,[28] and human glioblastoma cell line T98G (cat. no. CRL-1690) were obtained from the American Type Culture Collection (Manassas, VA, USA). Immortalized human retinal pigment epithelial cell line stably expressing telomerase reverse transcriptase hTERT-RPE1 (RPE1) was obtained from Dr. M. Bonhivers (Université Bordeaux; Bordeaux, France). Human cervical adenocarcinoma (HeLa) cells were kindly provided by the Institute of Experimental Medicine, Czech Academy of Sciences, and by Dr. Mělková from the First Faculty of Medicine, Charles University in Prague. A stable cell line of mouse bone marrow-derived mast cells (BMMCs) was donated by Dr. M. Hibbs (Ludwig Institute for Cancer Research, Melbourne, Australia).[29] T98G, RPE1, and HeLa cells were maintained in Dulbecco's modified Eagle's medium (DMEM; Lonza; Walkersville, MD, USA) containing 10% fetal bovine serum and antibiotics (100 U ml^{-1} penicillin and 0.1 mg ml^{-1} streptomycin). RBL cells were cultivated in 1 : 1 mixture of RPMI 1640 (Sigma-Aldrich) and DMEM media supplemented with serum and antibiotics. BMMCs were cultivated in RPMI 1640 medium supplemented with serum and antibiotics. Cells were grown at 37 °C under 5% CO_2 in the air and passaged every 2–3 days. RBL and BMMC cells were specifically activated by antigen (DNP-albumin). Cells were first sensitized with Ab SPE-7 (IgE) to DNP (Sigma-Aldrich, cat. no. D8406; 1 μg ml^{-1}) for 2 h in serum-free DMEM. IgE-sensitized cells were washed and activated with DNP-albumin (30–40 mol DNP per mol albumin; 100 ng ml^{-1}) for 3–60 min in Tyrode's buffer or RPMI 1640 medium without phenol red.

Cytotoxicity assay

HeLa, BMMC, and RBL cells were seeded onto 96-well flat bottom plate at a density 10×10^3 cells per well. After 24 h, an aqueous dispersion of GdF_3@PSSMA or GdF_3@PSSMA-PSDA-A488 particles (10 μl; 0–100 μg ml^{-1}) was added to cells in complete growth medium (100 μl). The incubation with the nanoparticles continued for 24 h and cell viability was measured using a Presto Blue cell viability reagent (Thermo Fisher Scientific) according to the manufacturer's instructions. Briefly, Presto Blue solution (10 μl) was added to cells at 37 °C for 3.5 h in an incubator with 5% CO_2 atmosphere and the fluorescence intensity was measured using a Synergy H1 Hybrid Reader (BioTek Instruments; Winooski, VT, USA) with excitation and emission at 550 and 590 nm, respectively. Data were expressed as the percentage of viable cells in the particle-treated group compared to the untreated group (control).

Degranulation assay and determination of intracellular Ca^{2+} concentration

The degree of degranulation was quantified as the release of β-hexosaminidase from anti-DNP IgE-sensitized RBL-2H3 or BMMC cells activated with antigen for 30 min using 4-NAG as a substrate.[30] The total content of enzyme was evaluated in supernatants from cells lysed by 0.1% Triton X-100. The extent of degranulation was calculated as follows: absorbance of culture supernatant × 100/absorbance of total cell lysate and normalized to control cells. Changes in the level of free intracellular Ca^{2+} were measured using Fura-2-AM as a cell-permeant calcium reporter following the protocol for sample handling.[31] The intracellular free Ca^{2+} was measured in an Infinite M200 microplate reader (Tecan; Männedorf, Switzerland) as Fura emissions at 510 nm after excitation with 340 and 380 nm lasers at the indicated time points. After the measurement of the Ca^{2+} basic level, activation was triggered by the addition of antigen.

Gel electrophoresis and immunoblotting

Whole-cell lysates for gel electrophoresis (SDS-PAGE) were prepared as described earlier[32] and electrophoresis and immuno-

blotting were performed using standard protocols.[33] For immunoblotting, mouse Ab to phosphor-tyrosine (EMD Millipore; La Jolla, CA, USA; cat. no. 05-1050), rabbit Ab to phosphorylated Syk (human $Y^{525/526}$ equivalent to rat $Y^{519/520}$; Cell Signaling; Danvers, MA, USA; cat. no. 2710) and rabbit Ab to actin (Sigma-Aldrich; cat. no. A2066) were diluted 1 : 3000, 1 : 2000, and 1 : 50 000, respectively. Secondary anti-mouse (cat. no. W402B) and anti-rabbit (cat. no. W401B) antibodies conjugated with horseradish peroxidase (HRP; Promega Biotec; Madison, WI, USA) were diluted to 1 : 10 000. The HRP signal was detected with SuperSignal West Pico chemiluminescent reagent (Pierce; Rockford, IL, USA) and a LAS 3000 imaging system (Fujifilm; Düsseldorf, Germany).

Fluorescence microscopy and live cell imaging

The cells were fixed in formaldehyde/Triton X-100 as described earlier.[34] Non-adherent BMMCs were attached to fibronectin-coated coverslips. Cells on coverslip were overlaid with nanoparticles in cultivation media. Alternatively, RBL and BMMCs on coverslips were placed down on drop of cultivation media with nanoparticles. F-actin (microfilaments) was visualized using rhodamine phalloidin according to the manufacturer's directions. Samples were embedded in poly(vinyl alcohol) (MOWIOL 4-88; Calbiochem; San Diego, CA, USA) and examined with a Delta Vision Core system (Applied Precision; Issaquah, WA, USA) equipped with a 60×/1.42 NA oil objective. For live cell imaging, RBL-2H3 cells were grown on an 8-well glass-bottomed chamber slide (Ibidi; Gräfelfing, Germany). The cells were then incubated with WGA Alexa Fluor 555 conjugate (5 μg ml^{-1}) in DMEM and Hoechst 33342 (5 μg ml^{-1}) to visualize cellular membranes and DNA, respectively. The cells were then washed with PBS, transferred in FluoroBrite™ DMEM, supplemented with 25 mM HEPES, and cultivated with the nanoparticles (2 mg ml^{-1}) for 3, 5, 15, 30, and 60 min. Images were collected in 70 optical slices (0.1 μm steps and 40 μm pinhole size) with an Andor Dragonfly 503 spinning disc confocal system (Oxford Instruments; Abingdon, UK) equipped with a stage top microscopy incubator, solid-state lasers (405 nm 200 mW, 488 nm 150 mW, and 561 nm 100 mW), HC PL APO 63×/1.20 water objective, and Zyla 4.2 PLUS sCMOS 16-bit camera. For each experiment, at least 5 cells were imaged. The images were deconvoluted with Huygens Professional software v. 20.04 (Scientific Volume Imaging; Hilversum, the Netherlands) and processed with Imaris v. 9.6 visualization software (Oxford Instruments). In 3D-reconstruction, the following colors were applied: red, nanoparticles attached/penetrating the plasma membrane; green, nanoparticles localized into the cytoplasm; grey, plasma membrane; blue, nucleus.

Statistical analysis

The cytotoxicity was expressed as the mean ± standard error mean (S.E.M.) of two independent experiments performed in sextuplicate. One-way ANOVA with Dunnett's *post hoc* test and two-sided unpaired *t*-test was used for calculation of statistical significance. The degranulation was expressed as mean ± standard deviation (S.D.). The statistical significance was determined by two-tailed unpaired Student's *t*-test; * $p < 0.05$, ** $p < 0.01$, and *** $p < 0.001$. Statistical analysis was performed using GraphPad Prism 7.01 software.

Results and discussion

Synthesis and physicochemical characterization of GdF_3@EG and GdF_3@PSSMA nanoparticles

GdF_3 nanoparticles were synthesized in a one-pot reaction from $GdCl_3{\cdot}6H_2O$ in EG with PSSMA as a stabilizer. If EG alone was used as a solvent and capping agent, GdF_3@EG particles were obtained. Morphology, size, and particle size distribution of GdF_3@EG and GdF_3@PSSMA nanoparticles were analyzed by TEM (see ESI, Fig. S1† and Table 1). GdF_3@EG nanoparticles had various shapes, were polydisperse with size in the 5–40 nm range (D_n = 18 nm; Fig. S1a†), and possessed moderately positive ζ-potential (7 mV). To investigate the effect of stabilizer concentration on the size of GdF_3 particles, they were prepared with different amounts of PSSMA (1–15 mg ml^{-1}). The GdF_3@PSSMA particles were larger (D_n = 4 nm; Fig. S1b†) and with a broader particle size distribution ($Đ$ = 1.8; Table 1) at a low concentration of PSSMA (1 mg ml^{-1}) than those synthesized at 15 mg of PSSMA per ml (D_n = 3 nm; Fig. S1d†), which possessed a narrower particle size distribution ($Đ$ = 1.1; Table 1), because more nuclei, but smaller in size, could be stabilized with a higher concentration of the stabilizer.[35] The stabilization of the particles during their nucleation was prompted by hydroxyl groups of EG and/or sulfonate and carboxyl groups of PSSMA, facilitating its adsorp-

Table 1 TEM, DLS and XRD analysis of GdF_3-based nanoparticles

Particles	PSSMA (mg ml^{-1})	D_n (nm)	$Đ$	D_h (nm)	ζ-Potential (mV)	D_{XRD} (nm)	Crystal structure
GdF_3@EG	—	18	1.4	120	7	9	Hexagonal
GdF_3@PSSMA	1	4	1.8	96	−28	—	—
	5	3	2.4	110	−41	—	—
	15	3	1.1	69	−45	6	Orthorhombic
GdF_3@PSSMA-PSDA-A488	15	50[a]	—	98	−60	—	—

PSSMA – poly(4-styrenesulfonic acid-*co*-maleic acid); PSDA-A488 – poly(styrene-*grad*-2-dimethylaminoethyl acrylate)-*block*-poly(2-dimethylaminoethyl acrylate)-Atto 488; D_n – number-average particle diameter (TEM); $Đ$ – dispersity (TEM); D_h – hydrodynamic diameter (DLS); D_{XRD} – mean particle diameter from X-ray diffraction. [a] Aggregates of tiny particles.

tion on the particle surface and preventing additional particle growth and agglomeration. The relatively large size of the GdF_3@EG particles can be explained by the limited adsorption of EG on the nuclei surface, which agreed with previously reported data on EG-stabilized nanoparticles.[36–38] The hydrodynamic diameter of the GdF_3@PSSMA (D_h = 69–110 nm) and GdF_3@EG nanoparticles (D_h = 120 nm) indicated a small tendency to aggregation (Table 1). Changes in ζ-potential (from −28 to −45 mV) pointed to the presence of increasing amounts of PSSMA on the particle surface at a higher concentration of the stabilizer in the reaction mixture. The addition of increasing amounts of PSSMA in the reaction system effectively inhibited the growth of GdF_3 nanocrystals, which in turn resulted in a smaller size and a narrower particle size distribution. PSSMA was bound to the nanoparticle surface *via* a strong chelating interaction between carboxyl groups of the polymer and Gd^{3+} ions. PSSMA polyelectrolyte thus played two crucial roles; it not only provided functionalized nanoparticles with enhanced colloidal stability but also controlled the surface charge density and size of the particles.

The crystal structure of EG- and PSSMA-stabilized GdF_3 nanoparticles was examined by a powder X-ray diffraction (XRD) analysis (Fig. 1). GdF_3@EG particles crystallized in the hexagonal phase described by the $P6_3/mcm$ space group.[39] In contrast, GdF_3@PSSMA particles crystallized in the orthorhombic phase and the refined lattice parameters were slightly smaller than those in GdF_3@EG nanoparticles. The mean sizes of crystallites calculated from the peak width of primary GdF_3@EG and GdF_3@PSSMA nanoparticles reached 9 and 6 nm, respectively, confirming a good control of the particle size by using a PSSMA stabilizer. The differences between the sizes of particles according to TEM and those calculated from XRD indicated that EG- and PSSMA-stabilized GdF_3 nanoparticles can be combined in doublets or triplets during drying. Magnetic measurements of EG- and PSSMA-stabilized GdF_3 nanoparticles showed that they were paramagnetic at RT and no transition to a magnetically ordered state was observed with cooling down to 2 K (Fig. 2a). In the literature, the transition of GdF_3 to magnetically ordered state occurred at temperatures as low as 1.25 K,[40] although the onset of ferromagnetic interactions between Gd^{3+} ions generally takes place at <50 K.[41] Isothermal magnetization curves of GdF_3@EG and GdF_3@PSSMA nanoparticles at 2 and 300 K in magnetic fields ≤7 T showed that the particles reached saturation magnetization at <3.5 T (Fig. 2b). The minor variation of the specific magnetization reflected rather the changing content of the fluoride phase and diamagnetic coating; the saturation magnetization of GdF_3@EG and GdF_3@PSSMA particles at 2 K and magnetic field 7 T reached 168 and 157 $Am^2\ kg^{-1}$, respectively. The results indicated that the magnetic behavior did not depend on the distance between the particles and the magnetic interparticle interactions were absent. The data were also comparable to those reported previously for GdF_3 nanoparticles,[42] which potentially qualifies them for bioimaging and bioseparation.

The presence of functional groups on the GdF_3 nanoparticle surface was determined by ATR-FTIR spectroscopy (Fig. 3). The absorption bands of Gd–F were situated at 160–400 cm^{-1}, while EG and PSSMA generated the C–H stretching (2800–3000 cm^{-1}) and O–H stretching and bending vibrations (~3600–3000 and 1640–1636 cm^{-1}, respectively). In the fingerprint region, νC–O asymmetric stretching vibrations or bending vibrations of the C–H groups of EG were observed at 1126 or ~1456 and 725 cm^{-1}, respectively.[43,44] In the spectrum of GdF_3@PSSMA nanoparticles, the characteristic PSSMA peaks included the C–H bending (1410 cm^{-1}) and C═O stretching vibrations of maleic acid (1720 cm^{-1}), aromatic C═C vibrations of styrene (1636 cm^{-1}), S–O stretching in SO_3H (1178 cm^{-1}), antisymmetric and symmetric stretching vibrations in SO_3^- (1038 and 1010 cm^{-1}, respectively), and C–S stretching in 4-styrenesulfonic acid (638 cm^{-1}).[45] The relative absorption intensities from the sulfonic acid almost did not change, which suggests that the majority of sulfonate groups of PSSMA were still present under basic conditions. New peaks at ~752 and 498 cm^{-1} were ascribed to the out-of-plane bending vibrations of C–H groups in the monosubstituted aromatic rings[46] and Gd–O vibrations.[47] In the FTIR spectrum of GdF_3@PSSMA nanoparticles, band at 1578 cm^{-1} corresponding to COOH groups of PSSMA disappeared (Fig. 3b), indicating complete deprotonation of the carboxyl groups and their interaction with the nanoparticle surface. Moreover, intensities of the absorption peaks at ~1114 and 624 cm^{-1} ascribed to C–O and Gd–O vibrations,[48] respectively, were much higher compared to those of GdF_3@EG and PSSMA, confirming the interaction of the carboxyl groups with Gd^{3+} ions. The characteristic absorption bands in the FTIR spectra of

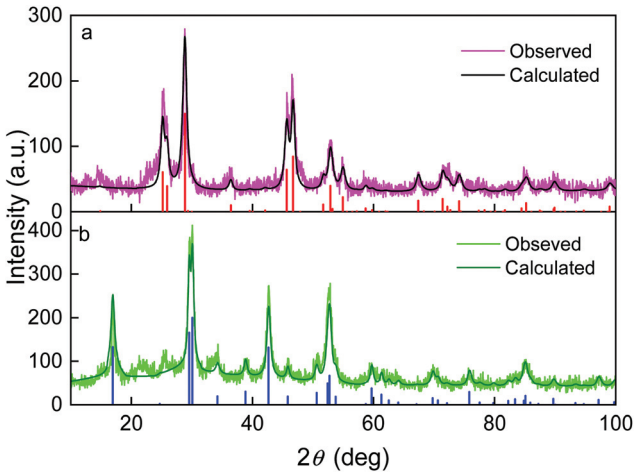

Fig. 1 XRD diffractograms of (a) GdF_3@EG and (b) GdF_3@PSSMA nanoparticles and comparison with calculated patterns. The vertical lines indicate diffractions of the hexagonal (red) and orthorhombic LnF_3 phases (blue). The original data retrieved from Inorganic Crystal Structure Database were based on the $P6_3/mcm$ of CeF_3 no. 42470 and *Pnma* of EuF_3 no. 95244 reflected by calculated patterns no. 01-074-3116 and 01-089-1933 in PDF, respectively.

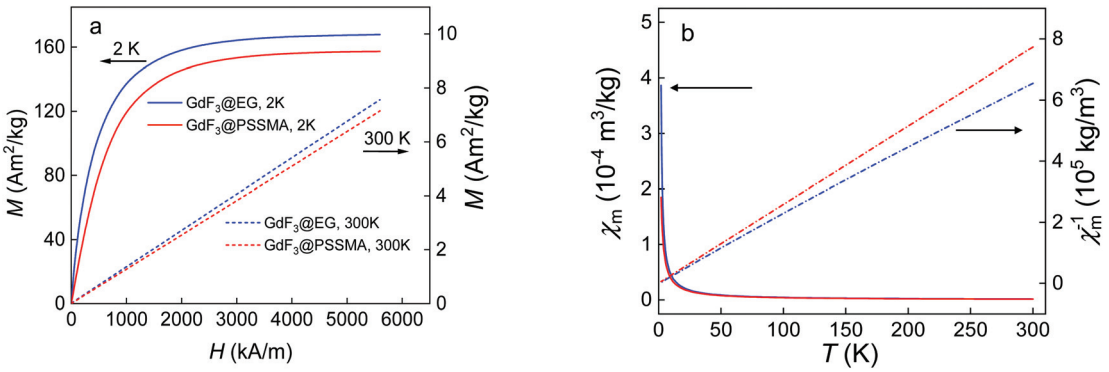

Fig. 2 (a) Magnetization curves of GdF_3@EG (blue) and GdF_3@PSSMA nanoparticles (red) at 2 (solid line) and 300 K (dot line) and (b) temperature dependence of mass magnetic susceptibility (χ_m; solid line) and inverse mass magnetic susceptibility of particles (χ_m^{-1}; dot line) measured at cooling in the applied magnetic field of 0.1 T.

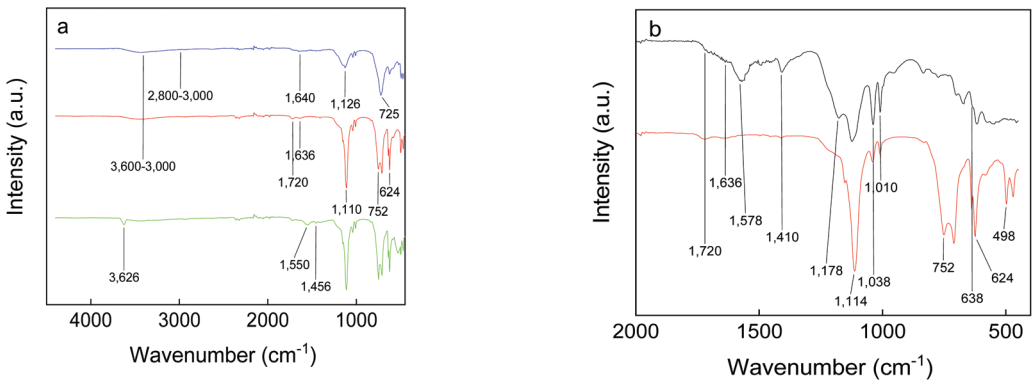

Fig. 3 FTIR spectra of PSSMA (black), GdF_3@EG (blue), GdF_3@PSSMA (red), and GdF_3@PSSMA-PSDA-A488 nanoparticles (green).

GdF_3@EG and GdF_3@PSSMA particles thus demonstrated the presence of EG and/or PSSMA coating.

Functionalization of GdF_3@PSSMA nanoparticles with PSDA-A488

To render PSSMA-stabilized GdF_3 nanoparticles prepared with 15 mg of PSSMA per ml luminescent, they were modified with fluorescent PSDA-A488 polymer (M_n = 14.5 kDa; polydispersity 1.2). PSDA is a novel pH- and thermo-responsive ion-sensitive amphiphilic diblock copolymer, built of hydrophilic poly(2-dimethylaminoethyl acrylate) (PDMAEA) and amphiphilic poly(styrene-*grad*-2-dimethylaminoethyl acrylate) [P(S-*grad*-DMAEA)] blocks (Scheme 1). PDMAEA was widely studied as a drug or gene delivery carrier, because of its low toxicity and high transfection efficiency.[49] TEM micrographs of the GdF_3@PSSMA-PSDA-A488 nanoparticles showed that they tended to aggregate during the surface modification and a moderately thick (~9 nm) and uniform PSDA-A488 coating layer was formed around small aggregates (~50 nm size; Fig. S1e†). Susceptibility of GdF_3@PSSMA-PSDA-A488 nanoparticles to aggregation was caused by electrostatic interactions between the positively charged amino groups of PSDA and the negatively charged sulfonate groups of PSSMA. In agreement with TEM data, DLS confirmed the increased hydrodynamic size of the GdF_3@PSSMA-PSDA-A488 nanoparticles (98 nm) in water compared to the D_h of GdF_3@PSSMA (69 nm) due to the presence of an additional PSDA layer. Functionalization of the particles with PSDA-A488 was also confirmed by their highly negative surface charge (ζ-potential = −60 mV; Table 1) originating from sulfonate groups of A488 dye. The hydrodynamic diameter of GdF_3@PSSMA-PSDA-A488 particles was determined also in the cell cultivation media with and without serum and in Tyrode's buffer reaching 100, 283, and 390 nm, respectively; such values are still in the nanoscale range.

Comparison between FTIR spectra of the nanoparticles before and after functionalization with PSDA-A488 demonstrated the successful modification due to the appearance of a peak at 1456 cm^{-1} ascribed to the $N(CH_3)_2$ deformational stretching in the spectrum of the GdF_3@PSSMA-PSDA-A488 nanoparticles (Fig. 3a). Additional bands at 3626 and 1550 cm^{-1} were attributed to N–H stretching and bending vibrations, respectively.

Modification of the GdF_3@PSSMA nanoparticles with PSDA-A488 was further corroborated by photoluminescence spectra of GdF_3@PSSMA-PSDA-A488 particles and PSDA-A488 (Fig. 4). After the excitation at 507 nm, the intense emission at 522 nm was assigned to A488. A shift of

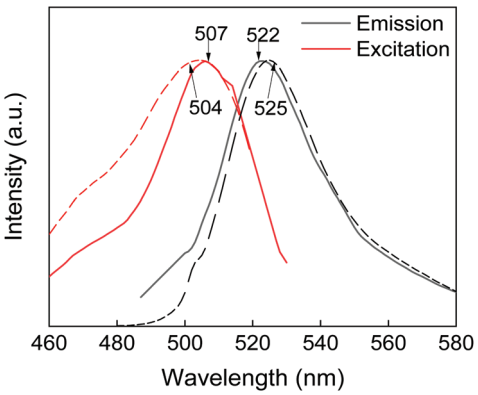

Fig. 4 Photoluminescence spectra of PSDA-A488 (dotted line) and GdF_3@PSSMA-PSDA-A488 nanoparticles (solid line).

GdF_3@PSSMA-PSDA-A488 peak (by 3 nm) from that of free PSDA-A488 was ascribed to the conjugation of PSDA-A488 to the nanoparticles.

Aqueous GdF_3@PSSMA-PSDA-A488 nanoparticle dispersion (3.7 mM of Gd^{3+}) stored at RT for 40 days was also examined for the release of toxic Gd^{3+} from the particles. A very low concentration of free Gd^{3+} ions (5.5 μM) was found in the supernatant (Fig. S2†), indicating negligible leaching from the particles and thus non-toxicity of the particles.

Cytotoxicity of GdF_3@PSSMA-PSDA-A488 nanoparticles

Effect of modification of GdF_3@PSSMA with PSDA-A488 on cell viability of adenocarcinoma cervical HeLa, BMMCs, and RBL mast cells was assessed with resazurin cell viability assay (Fig. 5). In the case of HeLa cells, their viability did not decrease after 24 h of incubation with both types of nanoparticles used in the range of concentrations 0–100 μg ml^{-1} (Fig. 5a). As a result, both GdF_3@PSSMA and GdF_3@PSSMA-PSDA-A488 particles can be considered non-toxic for these cells. However, in the case of RBL rat mast cells, GdF_3@PSSMA nanoparticles in the highest concentration (100 μg ml^{-1}) were weakly toxic according to international standards[50] with the cell viability within 80–60% ($p < 0.001$; Fig. 5c). In contrast, modification of the GdF_3@PSSMA nanoparticles with PSDA-A488 favorably reduced the cytotoxicity of particles and the RBL cell survival was >80%. Such viability is recognized by the International Organization for Standardization as non-toxic.[50] Non-cytotoxic behavior of GdF_3@PSSMA-PSDA-A488 towards mast cells were also confirmed on another mast cell line, BMMCs (Fig. 5b). GdF_3@PSSMA-PSDA-A488 decreased cell viability of BMMCs only by ~7.5% compared to the control. Moreover, the PSDA-A488 modification, similarly as in RBL cells, slightly reduced the cytotoxicity of GdF_3@PSSMA nanoparticles; the viability of cells incubated with GdF_3@PSSMA and GdF_3@PSSMA-PSDA-A488 increased from 90 to 92.5%. The results thus corroborate findings that the toxicity of free Gd^{3+} blocked by methylamide or hyaluronic acid is entirely suppressed.[24,51]

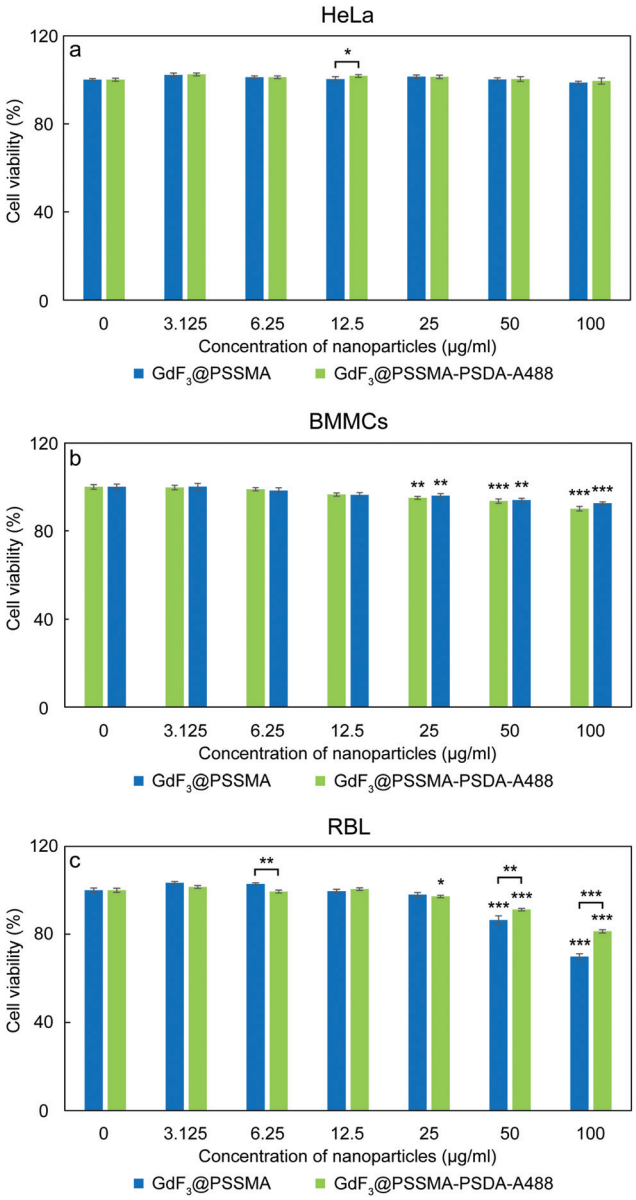

Fig. 5 Viability of (a) cervical adenocarcinoma HeLa, (b) bone marrow-derived mast cells BMMC, and (c) RBL mast cells after 24 h of incubation with GdF_3@PSSMA and GdF_3@PSSMA-PSDA-A488 nanoparticles. The values represent the mean ± standard error mean (S.E.M.) of two independent experiments performed in sextuplicate; * < 0.05, ** < 0.01, *** < 0.001 indicate statistical significance compared to control (one-way ANOVA with Dunnett's *post hoc* test) and significant difference in cell viability after exposure to the same concentration of GdF_3@PSSMA and GdF_3@PSSMA-PSDA-A488 particles (Student *t*-test).

Interference of GdF_3@PSSMA-PSDA-A488 nanoparticles with activation of mast cells and their degranulation

Specific activation of mast cells after the crosslinking of FcεRI receptor-bound IgE by multivalent allergens results in morphological changes and the release of mediators of the allergic response. We investigated the effect of GdF_3@PSSMA-PSDA-A488 nanoparticles on the morphology of

cells of different tissue origin including RBL cells and BMMCs by fluorescence microscopy. Increased cell spreading, delineated by phalloidin staining of F-actin, was detectable in RBL cells incubated with the particles. Morphological changes were detected in BMMCs as well. On the other hand, changes in cell morphology were not found in retinal pigment epithelial cells RPE1 and glioblastoma cells T98G (Fig. 6a). Morphological changes in RBL and BMMCs were observed after overlying cells with medium containing nanoparticles as well as after placing down cells, attached on a coverslip, on drop of medium with nanoparticles (not shown). This ruled out the possibility that changes were due to sinking of particles on cell surface. Prominent remodeling of microfilaments in RBL cells could reflect their activation with a typical temporal increase of overall protein tyrosine phosphorylation (P-Tyr) and activation of Syk kinase.[31] It was confirmed by examination of whole-cell lysates from RBL cells by immunoblotting that revealed the increase of P-Tyr and Syk activation, marked by phosphorylation of Syk (P-Syk [$Y^{525/526}$]) not only in the course of specific cell activation by antigen (see +Ag in Fig. 6a) but also during incubation with the nanoparticles (see +NPs in Fig. 6a). On the other hand, particles did not affect P-Tyr in RPE1 and T98G cells (Fig. 6b). Changes in P-Tyr indicated that the nanoparticles alone could interfere with signaling pathways characteristic for activated RBL cells.

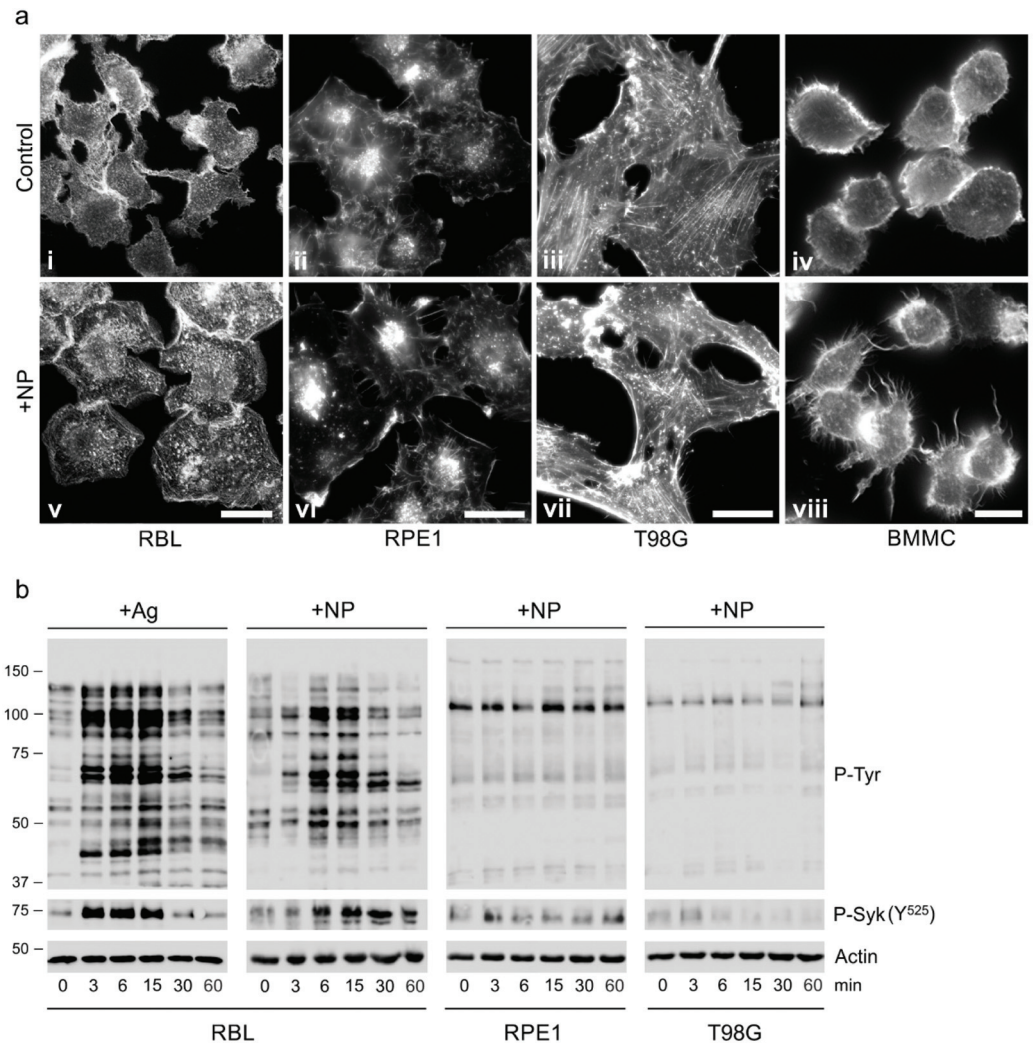

Fig. 6 Effect of GdF_3@PSSMA-PSDA-A488 nanoparticles (NPs) on cell morphology and protein tyrosine phosphorylation (P-Tyr) level in various cell lines. (a) Fluorescence micrographs of microfilaments in rat mast cell line RBL, human retinal pigment epithelial cell line RPE1, human glioblastoma cell line T98G, and mouse bone marrow-derived mast cell line BMMC in the absence (control) or presence of nanoparticles. RBL, RPE1, and T98G cells were incubated with the particles (2 mg ml^{-1}) for 15 min, fixed, and stained with rhodamine phalloidin. BMMCs were incubated with nanoparticles (1 mg ml^{-1}) for 5 min before fixation. The images (i and v), (ii and vi), (iii and vii), and (iv and viii) were collected and processed in the same manner. Scale bar (v–vii) 20 and (viii) 10 μm. (b) The immunoblot comparison of the P-Tyr and phosphorylation of Syk kinase (P-Syk[$Y^{525/526}$]) in whole-cell lysates from RBL, RPE1, and T98G cells incubated with the particles (2 mg ml^{-1}) for 0–60 min. Specific activation of IgE-sensitized (1 μg ml^{-1}) RBL cells with antigen (100 ng ml^{-1}; +Ag) represents the positive control (left). Actin served as the loading control. Representative images from three repetitions.

To test whether the elevation of P-Tyr level in RBL cells by GdF_3@PSSMA-PSDA-A488 nanoparticles alone can lead to sustained Ca^{2+} influx across the plasma membrane and to degranulation, the level of intracellular Ca^{2+} and β-hexosaminidase release was measured in the presence of different concentrations of particles. IgE-sensitized RBL cells activated by multivalent antigen served as a positive control. The Ca^{2+} influx was recorded only at the highest particle concentration. The Ca^{2+} level, however, reached only ~50% of that in control cells and was rapidly attenuated (Fig. 7a). The small increase in Ca^{2+} was not sufficient to initiate cell degranulation, measured by β-hexosaminidase release (Fig. 7b). These data demonstrated that the GdF_3@PSSMA-PSDA-A488 nanoparticles alone were not capable, even at the highest concentration (2 mg ml^{-1}), to induce sustained Ca^{2+} influx leading to degranulation in RBL cells. Similarly, the nanoparticles alone did not induce degranulation in BMMCs. However, the mechanism for effects of GdF_3@PSSMA-PSDA-A488 nanoparticles on mast cells is still unknown and warrants further investigation. On the other hand, concentration-dependent inhibition of Ca^{2+} mobilization (Fig. 7c) and degranulation (Fig. 7d) were observed in the presence of particles during activation of IgE-sensitized cells by antigen in adherent RBL cells. Similar interfering effect of particles on mast cell activation by FcεRI aggregation was also observed in non-adherent BMMCs that more closely resemble mast cells *in situ*. This was documented by Ca^{2+} mobilization (Fig. 8a) and degranulation (Fig. 8b). As the hydrodynamic diameter of particles increased in standard Tyrode's buffer used for the assay, the degranulation was also done in RPMI 1630 medium, where the nanoparticles have hydrodynamic diameter 100 nm. Under these conditions, the nanoparticles also showed inhibitory effects (Fig. S3†). These data suggested that the nanoparticles interfered with signaling cascades in the course of specific mast cell activation. Moreover, the overall P-Tyr level in antigen-activated cells was suppressed in the presence of nanoparticles (data not shown).

To visualize green fluorescence of nanoparticles by fluorescence microscopy on RBL cells or BMMCs, the cells were overlaid with cultivation media containing nanoparticles at concentration 0.1–2.0 mg ml^{-1} and incubated for 15 min. After

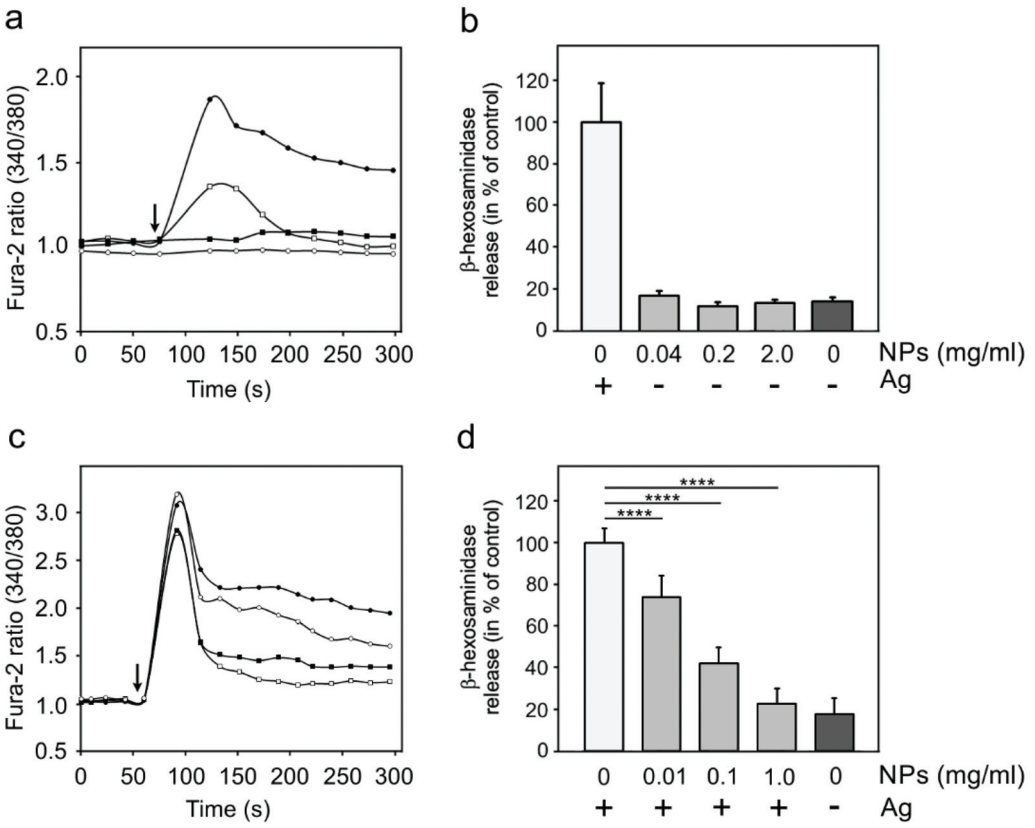

Fig. 7 Effect of GdF_3@PSSMA-PSDA-A488 nanoparticles (NPs) on calcium mobilization and degranulation in RBL cells. Calcium mobilization in (a) resting cells with added particles or (c) IgE-sensitized cells with added particles and antigen (Ag). Arrows in (a and c) indicate the time when antigen, nanoparticles alone, or particles with antigen were added. Fura-2-AM served as a cell-permeant calcium reporter. The typical experiments, out of three repetitions, are shown. (●) Positive control, (○) 0.01, (■) 0.1, and (□) 1 mg of particles per ml. Degranulation in (b) resting or (d) IgE-sensitized cells incubated with nanoparticles alone or particles with antigen for 30 min, respectively. Degranulation was measured by β-hexosaminidase release. The data represent the mean ± S.D. (n = 3) from the independent experiments performed in triplicates. Two-tailed unpaired Student's t test was performed to determine statistical significance. Activation of IgE-sensitized (1 μg ml^{-1}) cells by Ag (100 ng ml^{-1}) served in (a–d) as the positive control.

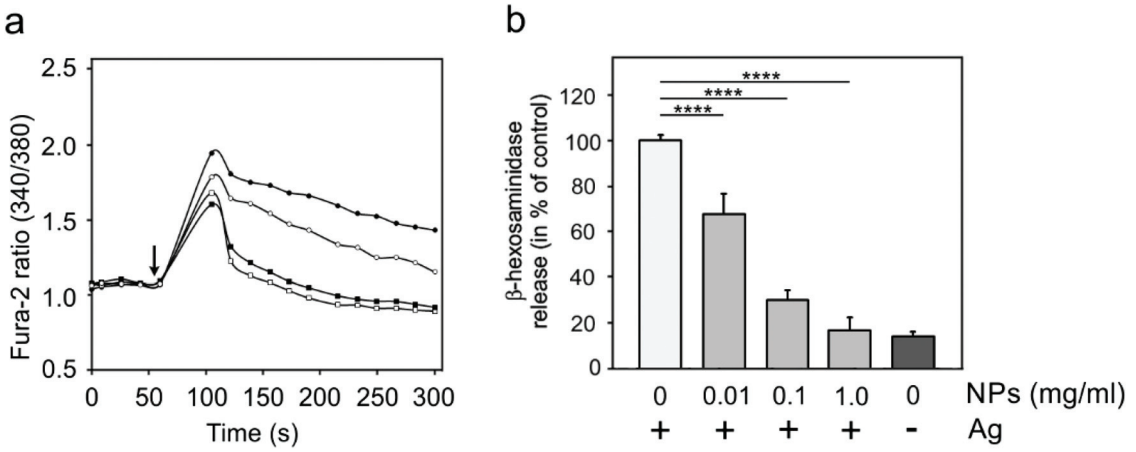

Fig. 8 Effect of GdF_3@PSSMA-PSDA-A488 nanoparticles (NPs) on calcium mobilization and degranulation in BMMCs. (a) Calcium mobilization in IgE-sensitized cells with added nanoparticles and antigen (Ag). Arrow indicates the time when antigen or particles with antigen were added. Fura-2-AM served as a cell-permeant calcium reporter. The typical experiment, out of three repetitions, is shown. (●) Positive control, (○) 0.01, (■) 0.1, and (□) 1 mg of particles per ml. (b) Degranulation in IgE-sensitized cells incubated with particles and antigen for 30 min measured by β-hexosaminidase release. The data represent the mean ± S.D. (n = 4) from the independent experiments performed in triplicates. Two-tailed unpaired Student's t test was performed to determine statistical significance. Activation of IgE-sensitized (1 μg ml^{-1}) cells by Ag (100 ng ml^{-1}) served in (a and b) as the positive control.

fixation, the preparations were stained for F-actin. While the morphological changes between control and nanoparticle-treated cells were clearly seen in RBL cells (Fig. 9a and b; rhodamine phalloidin staining), only very faint diffuse green fluorescence was detectable (Fig. 9c; fluorescence of nanoparticles). The similar results were obtained for BMMCs. On the other hand, when the cells were incubated with clustered nanoparticles (after more than 40 days of storage at concentration 20 mg ml^{-1}), bright green fluorescence was clearly detectable as shown by live cell imaging (Fig. 9d and e). Particles after 15 min of incubation were associated mainly with the plasma membrane, marked by WGA conjugate with Alexa Fluor 555 (Fig. 9d). After 60 min of incubation, the clustered particles were relocated intracellularly, as demonstrated in 3D cell reconstruction (Fig. 9e), not entering the nuclei. These results were in contrast to the literature, where uptake of 20 nm silver nanoparticles by mast cells was minimal.[23] As the GdF_3@PSSMA-PSDA-A488 nanoparticles attenuated P-Tyr (data not shown) and Ca^{2+} concentration 6 min after cell activation by antigen, when the degranulation was detectable, it is supposed that the particle internalization did not contribute to inhibition of degranulation.

The obtained data suggest that the GdF_3@PSSMA-PSDA-A488 nanoparticles bind to the RBL cell surface, interfere with signaling pathways initiated by cross-linking of FcεRIs with multivalent antigen, and suppress sustained Ca^{2+} mobilization. This results in the inhibition of mast cell degranulation, which usually initiates allergic and anaphylactic reactions reported in the case of carbon nanotubes, dendrimers, positively charged silica, and quantum dots.[52–54] The allergic reactions associated with exposure to contrast agent are known to be also induced in some patients, *e.g.*, by superparamagnetic iron oxide nanoparticles, which were approved and later declined by FDA and EMA for application as an *in vivo* contrast agent.[55,56] In this respect, GdF_3@PSSMA-PSDA-A488 nanoparticles might minimize mast cell degranulation and allergic responses. Inherent properties of the paramagnetic and luminescent GdF_3@PSSMA-PSDA-A488 nanoparticles, especially their ability to suppress mast cell degranulation, indicate that they may have therapeutic potential for the treatment of allergies and multimodal imaging.

Conclusions

GdF_3@PSSMA-PSDA-A488 nanoparticles represent a new platform for the construction of contrast agents with multiple imaging modalities and/or targeting capabilities. The morphology of particles (in particular, size) and crystallinity can be controlled by the reaction conditions involving steric stabilization with EG and/or PSSMA at different concentrations. The GdF_3-based core is paramagnetic with high longitudinal relaxivity in MRI, while PSSMA-PSDA-A488 shell confers luminescent characteristics on the nanoparticles, making them useful for optical fluorescence imaging. The combination of magnetic and fluorescent properties of GdF_3@PSSMA-PSDA-A488 nanoparticles can thus allow their applications in dual-mode imaging. The presence of amino groups of PSDA-A488 on the particle surface will make them accessible for additional conjugation with anticancer drugs, monoclonal antibodies, and/or photosensitizers that are important for the potential development of specific theranostic agents for multimodal bioimaging and drug delivery. GdF_3@PSSMA-PSDA-A488 nanoparticles are biocompatible and non-toxic towards adenocarcinoma HeLa, BMMCs, and RBL mast cells. Besides, the nanoparticles

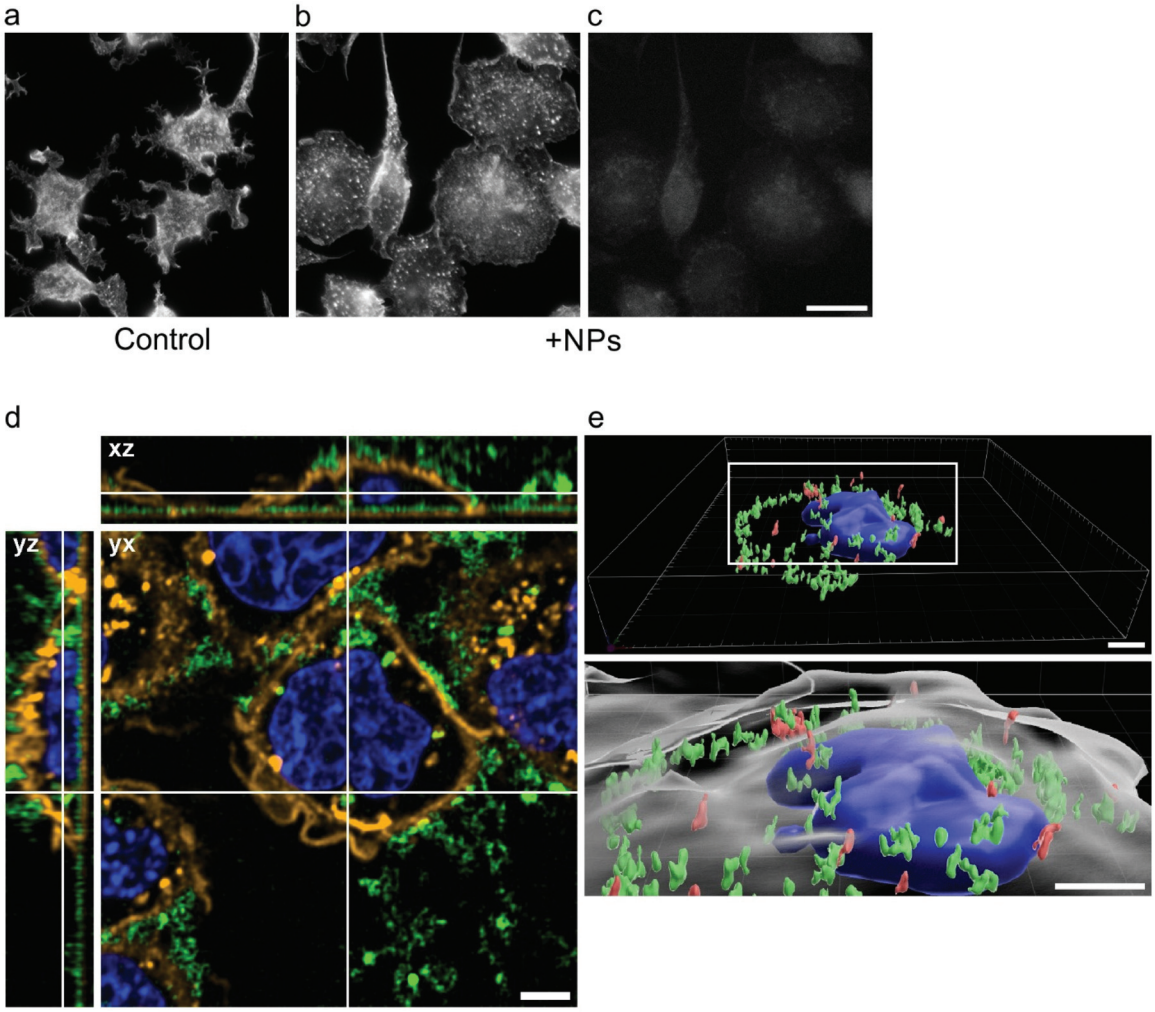

Fig. 9 Distribution of GdF_3@PSSMA-PSDA-A488 nanoparticles (NPs) in RBL cells. (a–c) Fluorescence micrographs of (a and b) microfilaments and (c) nanoparticles in the absence (a; control) and presence of nanoparticles (b and c). Cells were incubated with nanoparticles (2 mg ml^{-1}) for 15 min and after the fixation they were stained with rhodamine phalloidin; (b and c) represent the same cells. Scale bar 20 μm. (d) Still image and (e) 3D-reconstruction from live-cell imaging of RBL cells incubated with clustered nanoparticles (2 mg ml^{-1}) for (d) 15 min and (e) 60 min. (d) Nanoparticles (green), Alexa Fluor 555 conjugate of wheat germ agglutinin to mark cell membranes (orange), and Hoechst 33342 to label DNA in nuclei (blue). Top view (*yx*, single plane) and side views (*xz* and *yz*) from a z-stack. (e) 3D-reconstruction in the upper panel shows the nanoparticles attached/penetrating the plasma membrane (red) and localized into the cytoplasm (green) but not in the nucleus (blue). The boxed area is enlarged in the lower panel, where the plasma membrane is also depicted (grey). Scale bars 5 μm.

inhibit degranulation of RBL mast cells, probably due to the prevention of Ca^{2+} mobilization, which might favorably suppress allergic reactions after prospective *in vivo* administration improving immune tolerance of the nanoparticles. All these properties make multimodal GdF_3@PSSMA-PSDA-A488 nanoparticles safer and promising diagnostic tools useful for various applications, *e.g.*, monitoring of the biodistribution, blood circulation, and accumulation of drugs in the treatment of various severe disorders. As the GdF_3@PSSMA-PSDA-A488 nanoparticles suppress mast cell degranulation, they might minimize potential allergic reactions. They could be also suitable for investigations of signaling pathways during mast cell activation and the development of new strategies for the treatment of allergic diseases.

Conflicts of interest

There are no conflicts to declare.

Acknowledgements

Support of the Czech Science Foundation (no. 19-00676S and 18-27197S), Light Microscopy Service Laboratory (LM2018129 from MEYS), and Institutional Research Support (RVO 68378050) are acknowledged. We thank Dr. M. Hibbs (Ludwig Institute for Cancer Research, Melbourne, Australia) for the BMMC cell line and Dr. M. Bonhivers (Université Bordeaux, Bordeaux, France) for RPE1 cells.

Notes and references

1 D. Bekah, D. Cooper, K. Kudinov, C. Hillc, J. Seuntjens, S. Bradforth and J. Nadeau, Synthesis and characterization of biologically stable, doped LaF_3 nanoparticles co-conjugated to PEG and photosensitizers, *J. Photochem. Photobiol. A*, 2016, **329**, 26–34.

2 X. Zhu, J. Zhang, J. Liu and Y. Zhang, Recent progress of rare-earth doped upconversion nanoparticles: Synthesis, optimization and applications, *Adv. Sci.*, 2019, **6**, 1901358.

3 D. M. Samhadaneh, G. A. Mandl, Z. Han, M. Mahjoob, S. C. Weber, M. Tuznik, D. A. Rudko, J. A. Capobianco and U. Stochaj, Evaluation of lanthanide-doped upconverting nanoparticles for *in vitro* and *in vivo* applications, *ACS Appl. Bio Mater.*, 2020, **3**, 4358–4369.

4 E. N. M. Cheung, R. D. A. Alvares, W. Oakden, R. Chaudhary, M. L. Hill, J. Pichaandi, G. C. H. Mo, C. Yip, P. M. Macdonald, G. J. Stanisz, F. C. J. M. van Veggel and R. S. Prosser, Polymer-stabilized lanthanide fluoride nanoparticle aggregates as contrast agents for magnetic resonance imaging and computed tomography, *Chem. Mater.*, 2010, **22**, 4728–4739.

5 Y. Wang, R. Song, K. Guo, Q. Meng, R. Zhang, X. Kong and Z. Zhang, A gadolinium(III) complex based dual-modal probe for MRI and fluorescence sensing of fluoride ions in aqueous medium and in vivo, *Dalton Trans.*, 2016, **45**, 17616–17623.

6 W. Mnasri, M. Parvizian and S. Ammar-Merah, Design and synthesis of luminescent lanthanide-based bimodal nanoprobes for dual magnetic resonance (MR) and optical imaging, *Nanomaterials*, 2021, **11**, 354.

7 R. K. Sharma, A. V. Mudring and P. Ghosh, Recent trends in binary and ternary rare-earth fluoride nanophosphors: How structural and physical properties influence optical behavior, *J. Lumin.*, 2017, **189**, 44–63.

8 N. Halttunen, F. Lerouge, F. Chaput, M. Vandamme, S. Karpati, S. Si-Mohamed, M. Sigovan, L. Boussel, E. Chereul, P. Douek and S. Parola, Hybrid Nano-GdF_3 contrast media allows pre-clinical in vivo element-specific K-edge imaging and quantification, *Sci. Rep.*, 2019, **9**, 12090.

9 T. Passuello, M. Pedroni, F. Piccinelli, S. Polizzi, P. Marzola, S. Tambalo, G. Conti, D. Benati, F. Vetrone, M. Bettinelli and A. Speghini, PEG-capped, lanthanide doped GdF_3 nanoparticles: Luminescent and T_2 contrast agents for optical and MRI multimodal imaging, *Nanoscale*, 2012, **4**, 7682–7689.

10 S. Morsy, Role of surfactants in nanotechnology and their applications, *Int. J. Curr. Microbiol. Appl. Sci.*, 2014, **3**, 237–260.

11 S. Rodriguez-Liviano, N. O. Nunez, S. Rivera-Fernandez, J. M. de la Fuente and M. Ocana, Ionic liquid mediated synthesis and surface modification of multifunctional mesoporous Eu:GdF_3 nanoparticles for biomedical applications, *Langmuir*, 2013, **29**, 3411–3418.

12 M. Runowski and S. Lis, Nanocrystalline rare earth fluorides doped with Pr^{3+} ions, *J. Rare Earths*, 2016, **34**, 802–807.

13 F. Evanics, P. R. Diamente, F. C. J. M. van Veggel, G. J. Stanisz and R. S. Prosser, Water-soluble GdF_3 and GdF_3/LaF_3 nanoparticles - physical characterization and NMR relaxation properties, *Chem. Mater.*, 2006, **18**, 2499–2505.

14 Z. Shi, K. G. Neoh, E. T. Kang, B. Shuter and S.-C. Wang, Bifunctional Eu^{3+}-doped Gd_2O_3 nanoparticles as a luminescent and T_1 contrast agent for stem cell labeling, *Contrast Media Mol. Imaging*, 2010, **5**, 105–111.

15 K. Vuu, J. Xie, M. A. McDonald, M. Bernardo, F. Hunter, Y. Zhang, K. Li, M. Bednarski and S. Guccione, Gadolinium-rhodamine nanoparticles for cell labeling and tracking via magnetic resonance and optical imaging, *Bioconjugate Chem.*, 2005, **16**, 995–999.

16 D. Yang, Y. Zhao, H. Guo, Y. Li, P. Tewary, G. Xing, W. Hou, J. J. Oppenheim and N. Zhang, [Gd@C(82)(OH)(22)](n) nanoparticles induce dendritic cell maturation and activate Th1 immune responses, *ACS Nano*, 2010, **4**, 1178–1186.

17 E. Passante, C. Ehrhardt, H. Sheridan and N. Frankish, RBL-2H3 cells are an imprecise model for mast cell mediator release, *Inflammation Res.*, 2009, **58**, 611–618.

18 J. Kalesnikoff and S. J. Galli, New developments in mast cell biology, *Nat. Immunol.*, 2008, **9**, 1215–1223.

19 P. Dráber, V. Sulimenko and E. Dráberová, Cytoskeleton in mast cell signaling, *Front. Immunol.*, 2012, **3**, e130.

20 B. N. Feltis, A. Elbaz, P. F. Wright, G. A. Mackay, T. W. Turney and A. L. Lopata, Characterizing the inhibitory action of zinc oxide nanoparticles on allergic-type mast cell activation, *Mol. Immunol.*, 2015, **66**, 139–146.

21 H. Kang, S. Kim, K. H. Lee, S. Jin, S. H. Kim, K. Lee, H. Jeon, Y. G. Song, S. W. Lee, J. Seo, S. Park and I. H. Choi, 5 nm silver nanoparticles amplify clinical features of atopic dermatitis in mice by activating mast cells, *Small*, 2017, **13**, 1602363.

22 N. B. Alsaleh, I. Persaud and J. M. Brown, Silver nanoparticle-directed mast cell degranulation is mediated through calcium and PI3K signaling independent of the high affinity IgE preceptor, *PLoS One*, 2016, **11**, e0167366.

23 I. M. Yasinska, L. Calzolai, U. Raap, R. Hussain, G. Siligardi, V. V. Sumbayev and B. F. Gibbs, Targeting of basophil and mast cell pro-allergic reactivity using functionalised gold nanoparticles, *Front. Pharmacol.*, 2019, **10**, e333.

24 T. Kun and L. Jakubowski, Influence of MRI contrast media on histamine release from mast cells, *Pol. J. Radiol.*, 2012, **77**, 19–24.

25 M. Rabyk, A. Destephen, A. Lapp, S. King, L. Noirez, L. Billon, M. Hruby, O. Borisov, P. Stepanek and E. Deniau, Interplay of thermosensitivity and pH sensitivity of amphiphilic block-gradient copolymers of dimethylaminoethyl acrylate and styrene, *Macromolecules*, 2018, **51**, 5219–5233.

26 H. Hifumi, S. Yamaoka, A. Tanimoto, T. Akatsu, Y. Shindo, A. Honda, D. Citterio, K. Oka, S. Kuribayashi and K. Suzuki, Dextran coated gadolinium phosphate nanoparticles for magnetic resonance tumor imaging, *J. Mater. Chem.*, 2009, **19**, 6393–6399.

27 A. Barge, G. Cravotto, E. Gianolio and F. Fedeli, How to determine free Gd and free ligand in solution of Gd chelates. A technical note, *Contrast Media Mol. Imaging*, 2006, **1**, 184–188.
28 W. Alelwani, R. A. Alharbi, D. Wan, D. Vllasaliu, F. H. Falcone and S. Stolnik, Use of engineered nanoparticles (ENPs) for the study of high-affinity IgE FcεRI receptor engagement and rat basophilic leukemia (RBL) cell degranulation, *Basophils and Mast Cells, Methods in Molecular Biology*, 2020, **2163**.
29 M. L. Hibbs, D. M. Tarlinton, J. Armes, D. Grail, G. Hodgson, R. Maglitto, S. A. Stacker and A. R. R. Dunn, Multiple defects in the immune-system of Lyn-deficient mice, culminating in autoimmune-disease, *Cell*, 1995, **83**, 301–311.
30 K. Nishida, S. Yamasaki, Y. Ito, K. Kabu, K. Hattori, T. Tezuka, H. Nishizumi, D. Kitamura, R. Goitsuka, R. S. Geha, T. Yamamoto, T. Yagi and T. Hirano, FcεRI-mediated mast cell degranulation requires calcium-independent microtubule-dependent translocation of granules to the plasma membrane, *J. Cell Biol.*, 2005, **170**, 115–126.
31 Z. Hájková, V. Bugajev, E. Dráberová, S. Vinopal, L. Dráberová, J. Janáček, P. Dráber and P. Dráber, STIM1-directed reorganization of microtubules in activated cells, *J. Immunol.*, 2011, **186**, 913–923.
32 A. Klebanovych, V. Sládková, T. Sulimenko, V. Vosecká, Z. Rubíková, M. Čapek, E. Dráberová, P. Dráber and V. Sulimenko, Regulation of microtubule nucleation in mouse bone marrow-derived mast cells by protein tyrosine kinase SHP-1, *Cells*, 2019, **8**, e345.
33 V. Caracciolo, L. D'Agostino, E. Dráberová, V. Sládková, C. Crozier-Fitzgerald, D. P. Agamanolis, J. P. de Chadarevian, A. Legido, A. Giordano, P. Dráber and C. D. Katsetos, Differential expression and cellular distribution of ν-tubulin and βIII-tubulin in medulloblastomas and human medulloblastoma cell lines, *J. Cell Physiol.*, 2010, **223**, 519–529.
34 E. Dráberová and P. Dráber, A microtubule-interacting protein involved in coalignment of vimentin intermediate filaments with microtubules, *J. Cell Sci.*, 1993, **106**, 1263–1273.
35 S. Shen, E. D. Sudol and M. S. El-Aasser, Dispersion polymerization of methyl methacrylate: Mechanism of particle formation, *J. Polym. Sci., Part A: Polym. Chem.*, 1994, **32**, 1087–1100.
36 Q. Zhao, B. Shao, W. Lü, Y. Jia, W. Lv, M. Jiao and H. You, Ba_2GdF_7 nanocrystals: Solution-based synthesis, growth mechanism, and luminescence properties, *Cryst. Growth Des.*, 2014, **14**, 1819–1826.
37 J. Xu, S. Gai, P. Ma, Y. Dai, G. Yang, F. He and P. Yang, Gadolinium fluoride mesoporous microspheres: Controllable synthesis, materials and biological properties, *J. Mater. Chem. B*, 2014, **2**, 1791–1801.
38 F. N. Sayed, V. Grover, V. Sudarsan, B. N. Pandey, A. Asthana, R. K. Vatsa and A. K. Tyagi, Multicolored and white-light phosphors based on doped GdF_3 nanoparticles and their potential bio-applications, *J. Colloid Interface Sci.*, 2012, **367**, 161–170.
39 M. L. Afanasiev, S. P. Habuda and A. G. Lundin, The symmetry and basic structures of LaF_3, CeF_3, PrF_3 and NdF_3, *Acta Crystallogr., Sect. B: Struct. Crystallogr. Cryst. Chem.*, 1972, **28**, 2903–2905.
40 T. E. Katila, V. K. Typpi, G. K. Shenoy and L. Niinisto, Mössbauer studies of Gd^{3+} compounds at very low temperatures, *Solid State Commun.*, 1972, **11**, 1147–1150.
41 Y. C. Chen, J. Prokleska, W. J. Xu, J. L. Liu, J. Liu, W. X. Zhang, J. H. Jia, V. Sechovsky and M. L. Tong, A brilliant cryogenic magnetic coolant: Magnetic and magnetocaloric study of ferromagnetically coupled GdF_3, *J. Mater. Chem. C*, 2015, **3**, 12206–12211.
42 T. Grzyb, L. Mrówczyńska, A. Szczeszak, Z. Śniadecki, M. Runowski, B. Idzikowski and S. Lis, Synthesis, characterization, and cytotoxicity in human erythrocytes of multifunctional, magnetic, and luminescent nanocrystalline rare earth fluorides, *J. Nanopart. Res.*, 2015, **17**, 399.
43 L. G. Wade Jr., *Organic Chemistry*, Prentice Hall, New York, 4th edn, 1999, pp. 1208–1213.
44 R. S. Oliveira, B. S. Brito, J. Kulesza, S. Alves Jr. and B. S. Barros, Tunable photoluminescence of nanostructured $LaPO_4$:Eu^{3+}/Tb^{3+} synthesized via a microwave-assisted ethylene glycol route, *Ceram. Int.*, 2017, **43**, 8276–8283.
45 D. S. Kim, M. D. Guiver and S. Y. Nam, Preparation of ion exchange membranes for fuel cell based on crosslinked poly(vinyl alcohol) with poly(styrene sulfonic acid-*co*-maleic acid), *J. Membr. Sci.*, 2006, **281**, 156–162.
46 J. C. Yang, M. J. Jablonsky and J. W. Mays, NMR and FTIR studies of sulfonated styrene-based homopolymers and copolymers, *Polymer*, 2002, **43**, 5125–5132.
47 D. Stefanakis and D. F. Ghanotakis, Synthesis and characterization of gadolinium nanostructured materials with potential applications in magnetic resonance imaging, neutron-capture therapy and targeted drug delivery, *J. Nanopart. Res.*, 2010, **12**, 1285–1297.
48 V. V. Korolev, T. N. Lomova, D. V. Korolev, A. G. Ramazanova, E. G. Mozhzhukhina and E. N. Ovchenkova, New nanoscaled paramagnetic complexes, in *Advanced Environmental Analysis: Application of Nanomaterials*, ed. C. M. Hussain and B. Kharisov, Royal Society of Chemistry, Cambridge, 2016, vol. 2, pp. 14–47.
49 Y. Yang, F. Mo, Y. Chen, Y. Liu, S. Chen and J. Zuo, Preparation of 2-(dimethylamino)ethyl methacrylate copolymer micelles for shape memory materials, *J. Appl. Polym. Sci.*, 2015, **132**, 42312–42319.
50 ISO 10993-5:2009 Biological evaluation of medical devices. Part 5: Tests for *in vitro* cytotoxicity, International organization for standardization; Geneva, Switzerland, 2009.
51 M. Russo, P. Bevilacqua, P. A. Netti and E. Torino, A microfluidic platform to design crosslinked hyaluronic acid nanoparticles (cHANPs) for enhanced MRI, *Sci. Rep.*, 2016, **6**, 1–10.

52 U. C. Nygaard, J. S. Hansen, M. Samuelsen, T. Alberg, C. D. Marioara and M. Lovik, Single-walled and multi-walled carbon nanotubes promote allergic immune responses in mice, *Toxicol. Sci.*, 2009, **109**, 113–123.
53 T. Toyama, H. Matsuda, I. Ishida, M. Tani, S. Kitaba, S. Sano and I. Katayama, A case of toxic epidermal necrolysis-like dermatitis evolving from contact dermatitis of the hands associated with exposure to dendrimers, *Contact Dermatitis*, 2008, **59**, 122–123.
54 S. Jatana, B. C. Palmer, S. J. Phelan and L. A. DeLouise, Immunomodulatory effects of nanoparticles on skin allergy, *Sci. Rep.*, 2017, **7**, 3979.
55 V. M. Runge, Safety of approved MR contrast media for intravenous injection, *J. Magn. Reson. Imaging*, 2000, **12**, 205–213.
56 D. J. Korchinski, M. Taha, R. Yang, N. Nathoo and J. F. Dunn, Iron oxide as an MRI contrast agent for cell tracking, *Magn. Reson. Insights*, 2015, **8**, 15–29.